THE ASTROPHYSICAL JOURNAL, 498:716–727, 1998 May 10

PROCESSING OF ICY MANTLES IN PROTOSTELLAR ENVELOPES

J. E. CHIAR,[1] P. A. GERAKINES, AND D. C. B. WHITTET
Rensselaer Polytechnic Institute, Department of Physics, Applied Physics, and Astronomy, Troy, NY 12180
Y. J. PENDLETON AND A. G. G. M. TIELENS[2]
NASA-Ames Research Center, Mail Stop 245-3, Moffett Field, CA, 94035
A. J. ADAMSON
Centre for Astrophysics, University of Central Lancashire, Corporation Street, Preston PR1 2HE, England, UK
AND
A. C. A. BOOGERT
Kapteyn Astronomical Institute, P.O. Box 800, 9700 AV, Groningen, Netherlands
Received 1997 June 11; accepted 1997 December 16

ABSTRACT

We have obtained CO absorption profiles of several young stellar objects (YSOs), spanning a range of mass and luminosity, in order to investigate their ice mantle composition. We present the first detection of CO toward the class I YSO L1489 IRS in the Taurus dark cloud. In general, the CO profiles for YSOs show evidence for both processed and pristine ices in the same line of sight; strong indirect evidence for CO_2 is suggested in R CrA IRS 7, L1489 IRS, Elias 18, and GL 961E. Toward other sources (R CrA IRS 1, IRS 2, W33A, NGC 7538 IRS 9, Mon R2 IRS 2) CO is present in (nearly) pure form. We propose an evolutionary scenario to explain the chemical diversity of the icy mantles toward these objects.

Subject headings: dust, extinction — infrared: ISM: lines and bands — ISM: molecules — stars: evolution — stars: pre–main-sequence

1. INTRODUCTION

Molecules frozen on interstellar grain mantles can drive a rich gas-phase chemistry when outgassed in the heated regions around protostars (Charnley, Tielens, & Millar 1992). Thus, sight lines toward young stellar objects (YSOs) may contain thermally or energetically processed dust in addition to a cold undisturbed intracloud component. The 4.5–4.8 μm spectral region provides two potential diagnostics of radiative or thermal processing of interstellar ices in the environs of embedded stars in molecular clouds. A broad absorption feature centered at 4.62 μm is seen in the spectra of several YSOs and attributed to C≡N bonds in a nitrile or isonitrile ("XCN"; Lacy et al. 1984; Tegler et al. 1993, 1995; Pendleton et al. 1998). Laboratory studies have produced a similar feature by ultraviolet photolysis of CO and NH_3 (Lacy et al. 1984; Bernstein et al. 1995; Schutte & Greenberg 1997). Some proposed carriers are CH_3CN (Larson et al. 1985) and OCN^- (Grim & Greenberg 1987; Schutte & Greenberg 1997). The XCN feature has not yet been detected in the quiescent dark cloud medium. As CN-bearing solids in the laboratory are produced by energetic radiative processing of ices containing nitrogen, detection of this feature in YSOs is taken as evidence for (1) the presence of nitrogen in the unprocessed cloud ices, and (2) evolution of the ice in the vicinity of the embedded source. The adjacent feature at 4.67 μm, identified with solid CO, provides not only quantitative information on CO itself but also indirect evidence for the presence of other species such as O_2, N_2, and CO_2. Laboratory studies have shown that the position, width, and shape of the CO profile changes appreciably depending on temperature and the matrix in which the CO is frozen (e.g., Sandford et al. 1988; Gerakines et al. 1995). Detailed modeling of the CO feature has been accomplished by fitting laboratory ice analogs to the astronomical spectra (Tielens et al. 1991; Kerr, Adamson, & Whittet 1993; Chiar et al. 1994, 1995; Elsila, Allamandola, & Sandford 1997). In general, the CO profile contains (1) a broad (polar) component (at $\sim$4.682 μm) attributable to CO in a matrix dominated by H_2O and (2) a narrow (nonpolar) component (at $\sim$4.673 μm) produced by either pure CO, CO in a nonpolar matrix (such as CO mixed with CO_2, N_2, or O_2), or CO in a weakly polar matrix (i.e., CO mixed with a small amount of H_2O).

Field stars, located by chance alignment behind dark clouds, probe the quiescent cloud medium; their spectra provide a benchmark for comparison to YSO spectra. Toward field stars, the CO profile reflects the presence of cold (10 K) unprocessed ices dominated by CO itself or by CO in a nonpolar mixture (Chiar et al. 1994, 1995). The polar component makes only a small contribution to the overall profile. In contrast, CO features toward some embedded YSOs are relatively broad and show evidence for irradiated and/or warm ($T \geq 30$ K) ices (e.g., Palumbo & Strazzulla 1993). Detailed comparison to laboratory spectra shows that the CO profiles observed in a subset of these YSOs are consistent with the presence of CO:CO_2 mixtures. The existence of CO_2 in processed ices near embedded objects has long been suspected (as it is produced easily in the laboratory by UV irradiation of CO-rich or CH_3OH-rich ices; see d'Hendecourt et al. 1986; Allamandola, Sandford, & Valero 1988; Gerakines, Schutte, & Ehrenfreund 1996) and this was recently confirmed by data from the *Infrared Space Observatory* (*ISO*; de Graauw et al. 1996). Pure CO_2 begins to sublime at $\sim$45 K and can survive at even higher temperatures when mixed with other molecules (Sandford & Allamandola 1990), so it can exist under condi-

[1] Present address: NASA-Ames Research Center, Mail Stop 245-3, Moffett Field, CA, 94035.
[2] Present address: Kapteyn Astronomical Institute, P.O. Box 800, 9700 AV, Groningen, Netherlands.

TABLE 1

YOUNG STELLAR OBJECTS: LOG OF OBSERVATIONS WITH UKIRT

Source	Other Designation	Right Ascension (1950)	Declination (1950)	Date	Standard
W33A.....	...	18 11 44.6	−17 52 57	1995 Sep 15	BS 7120 (K1 II)
L1489 IRS	IRAS 04016+2610	04 01 40.6	+26 10 49	1995 Oct 31	SAO 76461 (F1 V)
R CrA IRS 1.....	TS 2.6, HH100 IR	18 58 28.3	−37 02 27	1996 Apr 28	BS 7254 (A2 V)
R CrA IRS 2.....	TS 13.1	18 58 19.1	−37 02 48	1995 May 18	SAO 210781 (F2 V)
R CrA IRS 7.....	R1	18 58 33.3	−37 01 45	1996 Apr 28	BS 7254 (A2 V)

NOTE.—Units of right ascension are hours, minutes, and seconds, and units of declination are degrees, arcminutes, and arcseconds.

tions where the more volatile CO, which sublimes at ~17 K in pure form, would be evaporated (or processed into other species). Recent *ISO* results show that CO_2 is also present in quiescent environments sampled by field stars (Whittet et al. 1998), but this is not evident from their CO profiles (Chiar et al. 1995), indicating that CO and CO_2 are not intimately mixed in the same ice layers in quiescent regions.

Extensive previous studies of ices in the nearby low to intermediate mass star-forming regions of Taurus, ρ Oph, Serpens, and R CrA clouds are reviewed by Chiar (1997a). In the present paper we present new observations of YSOs in the Taurus and R CrA clouds. Taurus-Auriga and Corona Australis reside at distances of 140 pc (Elias 1978) and 130 pc (Marraco & Rydgren 1981), respectively. Taurus, first surveyed in the near infrared by Elias (1978), extends over many degrees (several tens of parsecs). It is fragmentary in appearance with no well-defined center, and star formation has occurred in widespread regions throughout the cloud (Elias 1978). The Corona Australis complex is similar in extent and morphology to Taurus. Like Taurus, this cloud appears quiescent in nature; star formation within the cloud has not been triggered by external shock waves (Burton 1992). The core associated with R CrA, first surveyed by Taylor & Storey (1984), contains a cluster of young pre–main-sequence stars. Water ice and solid CO have been previously detected in Taurus by Whittet et al. (1983) and Whittet, Longmore, & McFadzean (1985) and in R CrA by Whittet & Blades (1980), Graham & Chen (1991), Chen & Graham (1993), and Tanaka et al. (1994). The threshold visual extinctions for detection of the these features are $A_V \sim 3$ mag (H_2O ice; Whittet et al. 1988; Chen & Graham 1993; Whittet et al. 1996) and ~6 mag (solid CO; Whittet et al. 1989; Chiar et al. 1995; Tanaka et al. 1994) for the dark clouds discussed in this work. These are comparable to the thresholds estimated for the Serpens dark cloud (Eiroa & Hodapp 1989; Chiar et al. 1994; Chiar 1997b);

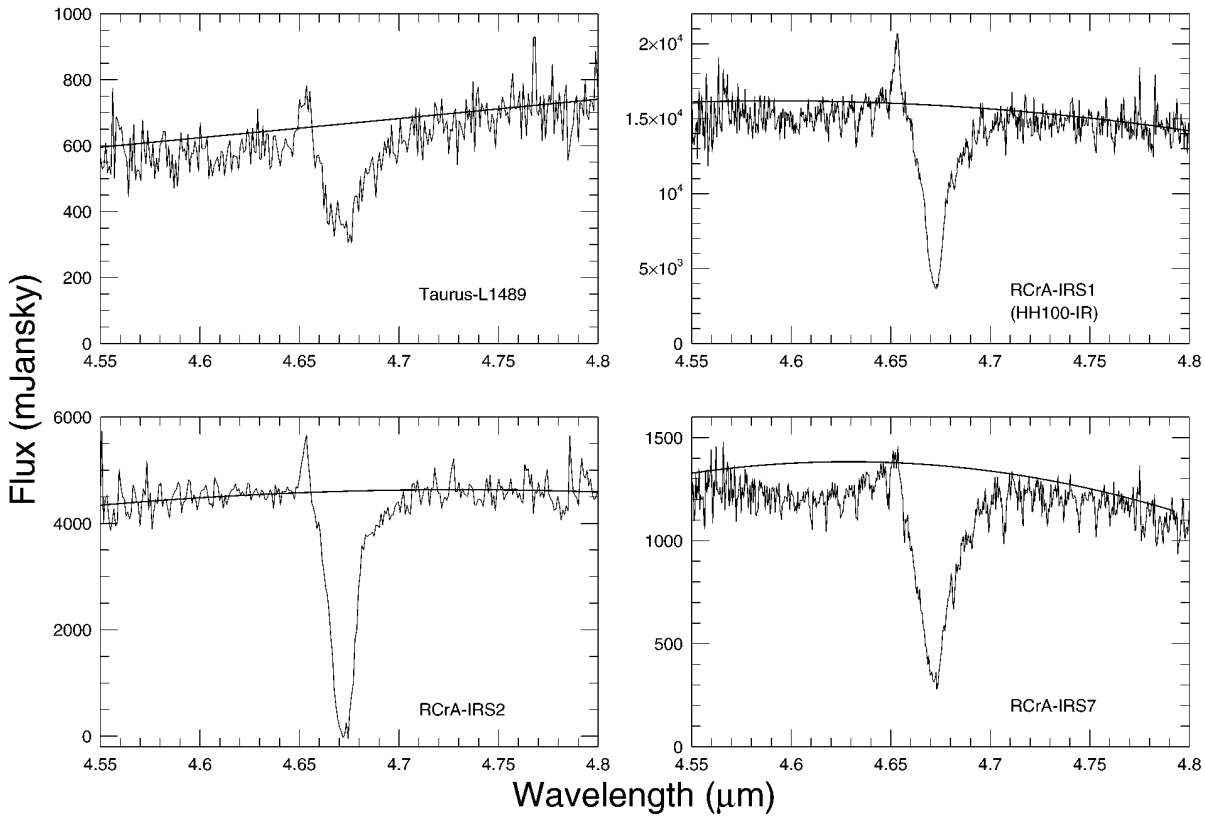

FIG. 1.—Flux-calibrated spectra shown with fitted second-degree polynomial continua. *Upper left*, Taurus L1489; *upper right*, R CrA IRS 1; *lower left*, R CrA IRS 2; and *lower right*, R CrA IRS 7. The CO feature of R CrA IRS 2 is saturated. The Pfβ emission feature at 4.654 μm is present in the spectra of L1489 IRS, R CrA IRS 1, and IRS 2.

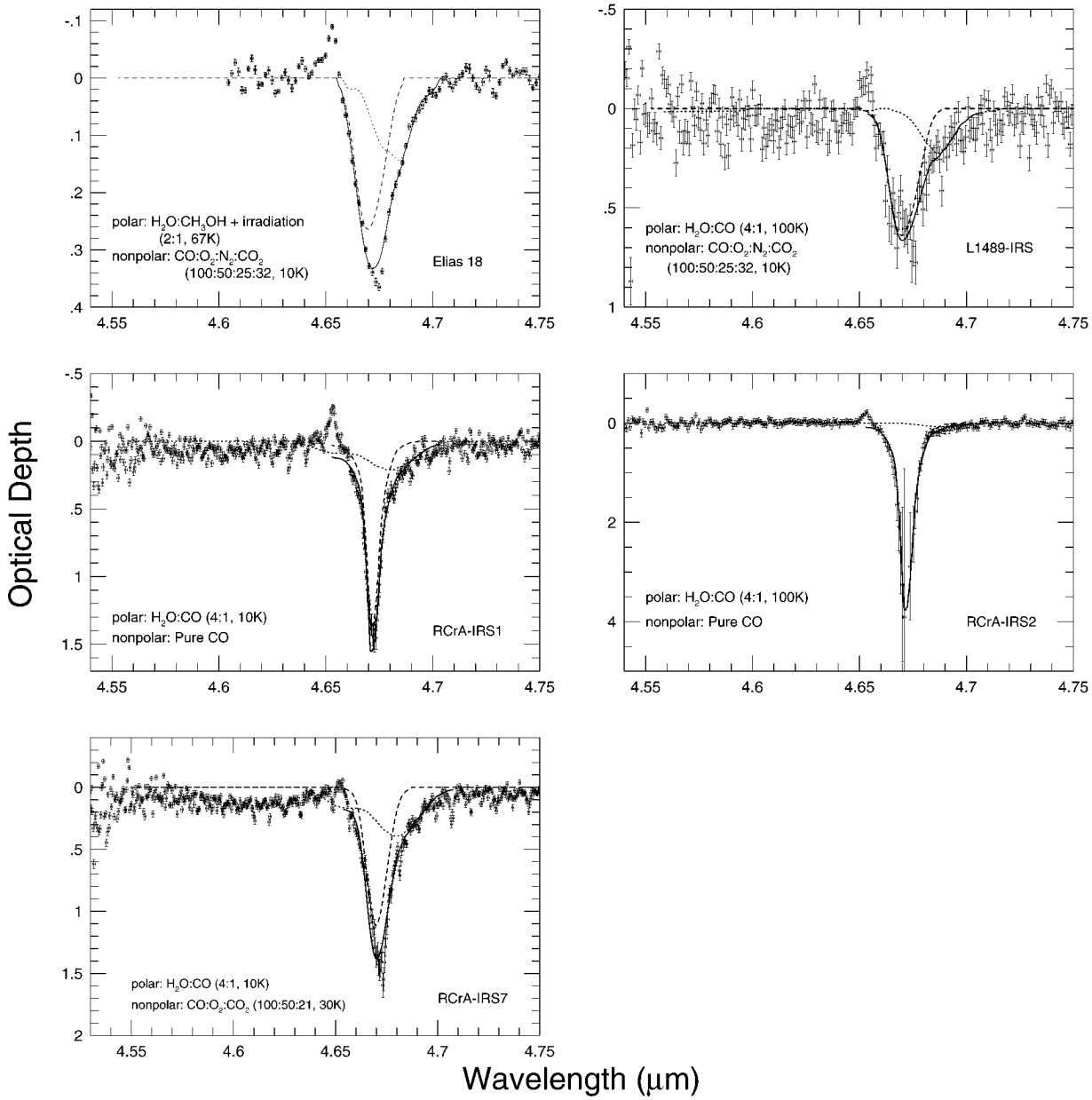

FIG. 2.—CO profiles for low-mass young stellar objects. Polar and nonpolar components are represented by dotted and dashed lines, respectively. The solid line represents the combination of the two components. *Upper left*, Taurus-Elias 18 (Chiar et al. 1995); *upper right*, Taurus L1489; *middle left*, R CrA IRS 1; *middle right*, R CrA IRS 2; *lower left*, R CrA IRS 7. The Pfβ emission feature at 4.654 μm is present in the spectra of Elias 18, L1489 IRS, R CrA IRS 1, and IRS 2.

much higher extinctions are required to detect (CO and H_2O) ice features in the ρ Oph dark cloud (Tanaka et al. 1990; Kerr et al. 1993).

Water ice and CO have also been detected in high-mass star-forming regions such as W33, GL961, NGC7538, and Monoceros R2 (Smith, Sellgren, & Tokunaga 1989; Geballe 1986; Tielens et al. 1991). In general, YSOs in these cloud cores are surrounded by reflection nebulosity and are heavily embedded, suffering anywhere from 17–150 mag of extinction (see Table 6). Because of uncertainties in visual extinction estimates toward these objects, calculation of threshold values has not been attempted; however, they are likely to be several times higher than the low-mass star-forming regions discussed above. Observations in the 4.5–4.8 μm spectral region of YSOs in low- and high-mass star-forming regions are presented in § 2. The routine used to fit the CO profiles is described in § 3; results for individual objects are discussed in the following sections (§§ 4 and 5). Finally, we propose an evolutionary scenario, which may explain the diverse composition of ices around embedded objects, in § 6, and we summarize our results in § 7.

2. OBSERVATIONS

New observations of Taurus L1489 IRS, R CrA IRS 1, R CrA IRS 2, and R CrA IRS 7 were carried out with the 256 × 256 InSb array of the cooled grating spectrometer CGS4 on the United Kingdom Infrared Telescope (UKIRT) on Mauna Kea. The spectrum of L1489 IRS was obtained on 1995 October. The spectrum of R CrA IRS 2 was obtained during service time in 1995 May. The spectra of R CrA IRS 1 and R CrA IRS 7 were obtained during service time in 1996 April. Details of the individual obser-

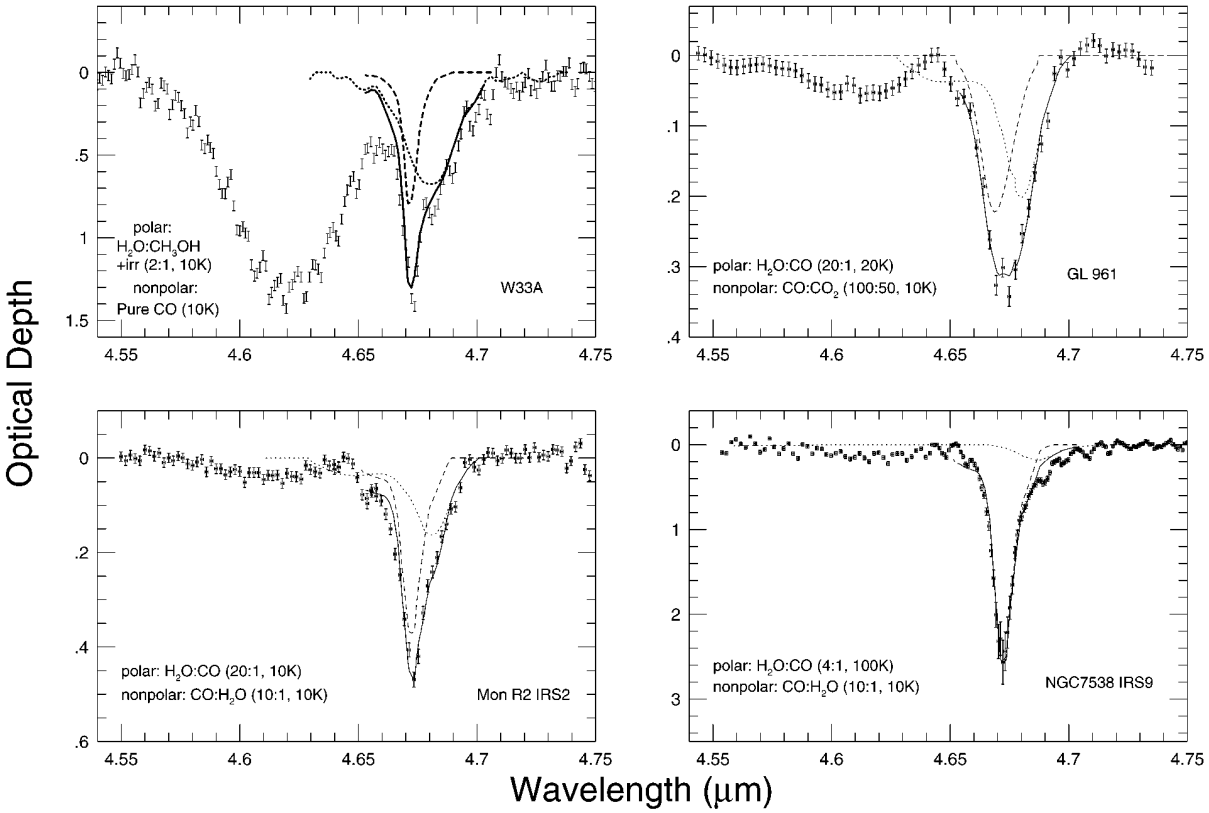

FIG. 3.—CO profiles for high-mass young stellar objects. Polar and nonpolar components are represented by dotted and dashed lines, respectively. The solid line represents the combination of the two components. *Upper left*, W33A; *upper right*, GL 961E; *lower left*, Mon R2 IRS 2; *lower right*, NGC 7538 IRS 9.

vations are listed in Table 1. For these sources, the short focal length (150 mm) camera and the 75 lines mm^{-1} grating were used providing a resolving power $(\lambda/\Delta\lambda) \sim 1800$. Wavelength calibration was achieved through comparison to an argon lamp. Cancellation of atmospheric telluric features and flux calibration was achieved by ratioing each program star with a standard star close in spectral type, observed at differential air mass ≤ 0.06. Each flux-calibrated spectrum (Fig. 1) was fitted with a second-degree continuum using the Starlink ABLINE routine. Narrow gas-phase CO absorption lines and the XCN feature (R CrA IRS 7) were not included in the continuum regions. Optical depth spectra ($\tau = -\ln F_{\rm source}/F_{\rm continuum}$) are shown in Figure 2.

To increase the sample of YSOs, we combine our new observations described above with previously published spectra of the same spectral region for Elias 18, W33A, GL 961E, Mon R2 IRS 2, and NGC 7538 IRS 9. W33A was observed in 1995 September with the spectropolarimetry module on CGS4 by A. Chrysostomou and coworkers (Chrysostomou et al. 1996). Data for Elias 18, obtained at UKIRT, are described in Chiar et al. (1995). Observations of GL 961E, Mon R2 IRS 2, and NGC 7538 IRS 9 were carried out, during two observing runs in 1986 November and 1988 July, by using the NASA Infrared Telescope Facility (IRTF) on Mauna Kea (Tielens et al. 1991). The cooled grating array spectrometer (CGAS) was used in first order with grating "B," giving a resolving power $(\lambda/\Delta\lambda) \sim 1200$. Details of the observations and data reduction are given in Tielens et al. (1991). The optical depth spectra are shown in Figure 3.

3. THE CO PROFILES AND XCN: EVIDENCE FOR PROCESSED GRAINS

Fits to the CO profile for all sources were carried out employing the χ^2 minimization method described in Kerr et al. (1993) and Chiar et al. (1995) using the nonpolar and polar laboratory mixtures listed in Table 2. The laboratory data are from Sandford et al. (1988), Schmitt, Greenberg, & Grim (1989), Palumbo & Strazzulla (1993), Tielens et al. (1991, hereafter TTGB), and Ehrenfreund et al. (1996). As particle shape affects the CO profile for CO concentrations more than 30% (Tielens et al. 1991), Mie scattering theory for homogeneous spheres was used to correct the laboratory profiles so that they may be compared to the astronomical spectra.[3] The details of these calculations are discussed elsewhere (TTGB; Ehrenfreund et al. 1997). TTGB found that a complex profile arises when core-mantle spheres with core/mantle volumes more than 0.3 are used; calculations for smaller core/mantle volumes replicate the homogeneous sphere case. The fits are not expected to change substantially if a continuous distribution of homogeneous ellipsoids is used (see TTGB). Thus, we chose to use calculations for homogeneous spheres in this work. Table 3 lists the peak optical depth ($\tau_{4.67}$), full width at half-maximum (FWHM), and central wavelength (λ_0) for the entire CO profile as determined from the fitting routine.

The two CO components are fitted simultaneously. The best-fitting combination of laboratory mixtures, their

[3] Optical constants for CO-rich ices are somewhat uncertain; the reader is referred to Ehrenfreund et al. (1997) for further discussion.

optical depths, and the corresponding χ_ν^2 for each fit are listed in Table 4. Although ideally a good fit should have $\chi_\nu^2 \sim 1$, in practice uncertainties in error-bar estimates (for the astronomical spectra) result in χ_ν^2 values somewhat larger than 1. Reduced χ^2 can also be made artificially small if the error bars of the observed data are large due to a poor signal-to-noise ratio or overestimation of the uncertainties. For each spectrum analyzed in this work, a list of all combinations of polar and nonpolar mixtures and the corresponding χ_ν^2 value was generated by the fitting routine. Starting from the lowest χ_ν^2 and progressing toward fits with higher χ_ν^2, each fit was visually inspected for quality. We found that several combinations of (polar and nonpolar) laboratory mixtures provided comparable matches to each astronomical spectrum (see Table 5). When the best χ_ν^2 value was less than 2, apparently satisfactory fits resulted for χ_ν^2 values within 20% of the lowest value. When χ_ν^2 for the best fit was greater than 2, acceptable fits resulted for χ_ν^2 within 30% ($2 < \chi_\nu^2 < 4$) and 40% ($\chi_\nu^2 > 5$) of the best fit. We illustrate these criteria in Figure 4, which shows the best fit to R CrA IRS 1 ($\chi_\nu^2 \sim 3.9$; *top*) compared to a fit that is just outside the 30% cutoff ($\chi_\nu^2 \sim 5.6$; *bottom*). The fit shown in the lower panel is obviously poor; the long-wavelength side of the feature is scarcely matched by the laboratory data.

TABLE 2

LABORATORY MIXTURES USED IN THIS WORK

Mixture	Ratio	T (K)	Reference
Polar Laboratory Mixtures			
CO_2:CO	(20:1)	10	1
H_2O:CO	(20:1)	10	1
H_2O:CO	(20:1)	20	1
H_2O:CO	(20:1)	30	1
H_2O:CO	(20:1)	40	1
H_2O:CO	(20:1)	50	1
H_2O:CO	(20:1)	65	1
H_2O:CO	(20:1)	80	1
H_2O:CO	(4:1)	10	2
H_2O:CO	(4:1)	25	2
H_2O:CO	(4:1)	35	2
H_2O:CO	(4:1)	50	2
H_2O:CO	(4:1)	100	2
H_2O:CH_3OH + irradiation	(2:1)	10	3
H_2O:CH_3OH + irradiation	(2:1)	67	3
Nonpolar Laboratory Mixtures			
Pure CO	...	10	4
CO:H_2O	(10:1)	10	4
CO:O_2	(2:3)	10	4
CO:O_2	(19:5)	10	4
CO_2:CO	(20:1)	10	4
Pure CO + irradiation	...	10	3
CO:CO_2 + UV	100:50	10	5
CO:CO_2 + UV	50:100	10	5
Pure CO	...	10	5
CO:H_2O	100:1	10	5
CO:O_2:H_2O	80:20:1	10	5
CO:O_2	100:50	10	5
CO:O_2	100:70	10	5
CO:O_2:H_2O	50:50:1	10	5
CO:O_2:H_2O	20:60:1	10	5
CO:CO_2	100:4	10	5
CO:CO_2	100:8	10	5
CO:CO_2	100:16	10	5
CO:CO_2	100:21	10	5
CO:CO_2	100:23	10	5
CO:CO_2	100:26	10	5
CO:CO_2:H_2O	50:56:1	10	5
CO:O_2:CO_2	100:50:4	10	5
CO:O_2:CO_2	100:50:8	10	5
CO:O_2:CO_2	100:50:16	10	5
CO:O_2:CO_2	100:50:21	10	5
CO:O_2:CO_2	100:50:32	10	5
CO:O_2:CO_2	100:54:10	10	5
CO:O_2:CO_2	100:20:11	10	5
CO:O_2:CO_2	100:11:20	10	5
CO:O_2:CO_2	100:10:23	10	5
CO:N_2:H_2O	50:50:1	10	5
CO:O_2:N_2	100:50:25	10	5
CO:O_2:N_2:H_2O	40:40:20:1	10	5
CO:N_2:CO_2	100:50:20	10	5
CO:O_2:N_2:CO_2	100:50:25:32	10	5
CO:O_2:N_2:CO_2:H_2O	50:35:15:3:1	10	5
CO:O_2:N_2:CO_2:H_2O	50:35:15:3:1	10	5
CO:O_2:N_2:CO_2:H_2O	25:25:10:13:1	10	5
Pure CO	...	30	5
CO:H_2O	100:1	30	5
CO:O_2:H_2O	80:20:1	30	5
CO:O_2	100:50	30	5
CO:O_2:H_2O	50:50:1	30	5
CO:O_2:H_2O	20:60:1	30	5
CO:CO_2	100:4	30	5
CO:CO_2	100:8	30	5
CO:CO_2	100:16	30	5
CO:CO_2	100:21	30	5
CO:CO_2	100:23	30	5
CO:CO_2	100:26	30	5
CO:CO_2:H_2O	50:56:1	30	5
CO:O_2:CO_2	100:50:16	30	5
CO:O_2:CO_2	100:50:21	30	5
CO:O_2:CO_2	100:54:10	30	5
CO:O_2:CO_2	100:10:23	30	5
CO:N_2:H_2O	50:50:1	30	5
CO:O_2:N_2:H_2O	40:40:15:1	30	5

REFERENCES.—(1) Sandford et al. 1988; (2) Schmitt et al. 1989; (3) Palumbo & Strazzulla 1993; (4) Tielens et al. 1991; (5) Ehrenfreund et al. 1996.

Gas-phase CO lines are present in the 4–5 μm spectra of many embedded objects. Figure 5 shows the well-studied clearly separated R and P branches of the strong gas-phase CO lines in the high-mass protostar GL 2591 (Tielens et al. 1991) compared to the spectrum of R CrA IRS 7. It is apparent that the narrow absorption lines in the spectrum of R CrA IRS 7 (and R CrA IRS 1; Fig. 2, *middle left*) are due to gas-phase CO. Gas-phase lines are also partially

TABLE 3

CO PROFILE PARAMETERS

Source	$\tau_{4.67}$	FWHM (cm^{-1})	λ_0 (μm)
Low-Mass Objects			
Elias 18	0.33 ± 0.03	9.48	4.672
L1489 IRS	0.7 ± 0.1	7.94	4.670
R CrA IRS 1	1.55 ± 0.05	3.67	4.671
R CrA IRS 2	4 ± 1	3.22	4.671
R CrA IRS 7	1.38 ± 0.05	6.12	4.671
High-Mass Objects			
W33A	1.30 ± 0.05	7.64	4.672
GL 961E	0.31 ± 0.03	10.76	4.675
Mon R2 IRS 2	0.47 ± 0.02	6.73	4.674
NGC 7538 IRS 9	2.6 ± 0.2	4.75	4.673

TABLE 4

BEST-FITTING LABORATORY MIXTURES FOR POLAR AND NONPOLAR COMPONENTS

SOURCE	NONPOLAR COMPONENT		POLAR COMPONENT		
	Mixture	τ	Mixture	τ	χ^2_ν
Low-Mass Objects					
Elias 18	$CO:O_2:N_2:CO_2$ (100:50:25:32, 10 K)	0.26 ± 0.03	$H_2O:CH_3OH$ + irr. (2:1, 67 K)	0.14 ± 0.03	5.6
L1489 IRS	$CO:O_2:N_2:CO_2$ (100:50:25:32, 10 K)	0.6 ± 0.1	$H_2O:CO$ (4:1, 100 K)	0.2 ± 0.1	1.7
R CrA IRS 1	Pure CO (10 K)	1.40 ± 0.05	$H_2O:CO$ (4:1, 10 K)	0.21 ± 0.05	3.9
R CrA IRS 2	Pure CO (10 K)	4 ± 1	$H_2O:CO$ (4:1, 100 K)	$0.01 \pm .01$	0.7
R CrA IRS 7	$CO:O_2:CO_2$ (100:50:21, 30 K)	1.12 ± 0.05	$H_2O:CO$ (4:1, 10 K)	0.39 ± 0.05	5.3
High-Mass Objects					
W33A	Pure CO	0.79 ± 0.05	$H_2O:CH_3OH$ + irr. (2:1, 10 K)	0.68 ± 0.05	6.1
GL 961E	$CO:CO_2$ + UV (100:50, 10 K)	0.22 ± 0.03	$H_2O:CO$ (20:1, 20 K)	0.20 ± 0.03	1.7
Mon R2 IRS 2	$CO:H_2O$ (10:1, 10 K)	0.37 ± 0.02	$H_2O:CO$ (20:1, 10 K)	0.16 ± 0.02	3.0
NGC 7538 IRS 9	$CO:H_2O$ (10:1, 10 K)	2.5 ± 0.2	$H_2O:CO$ (4:1, 100 K)	0.2 ± 0.1	3.0

resolved in the spectrum of Elias 18 (Fig. 2, *upper left*) and W33A (Fig. 3, *upper left*). In cases where the gas-phase lines are not separated, blending may cause a shallow absorption feature that mimics an XCN feature. For the spectra presented here, this effect can be ruled out since ample wavelength coverage is available on both sides of the solid-state CO feature. Gas-phase absorption (where present) could also have a minor affect on the fit to the CO profile. If gas-phase lines are not taken into account during the fitting procedure, the precise peak position of the polar component cannot be constrained and its depth may be slightly overestimated. In this work, great care was taken to exclude troublesome gas-phase lines centered at ~4.6810, 4.6892, 4.6989, 4.7067 μm, so as not to affect the fit to the solid-state

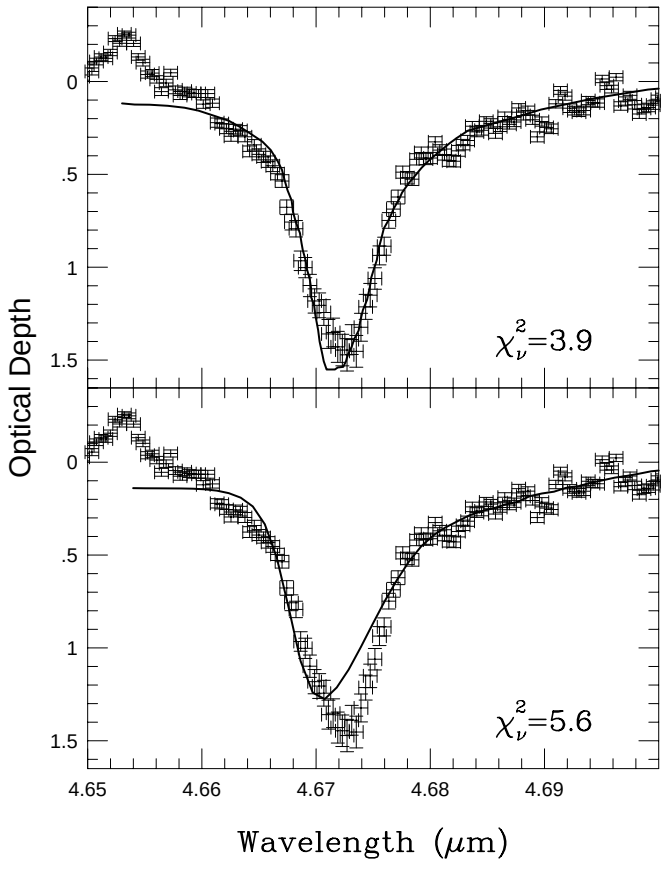

FIG. 4.—Best fit ($\chi^2_\nu = 3.9$) (*top*) compared to a poor fit ($\chi^2_\nu = 5.6$) (*bottom*) to spectrum of R CrA IRS 1. The "bad" fit is given by $H_2O:CO:O_2$ (1:50:50, 30 K) (nonpolar component) and $H_2O:CO$ (4:1, 10 K) (polar component). In both panels, the combination of polar and nonpolar components is represented by a solid line.

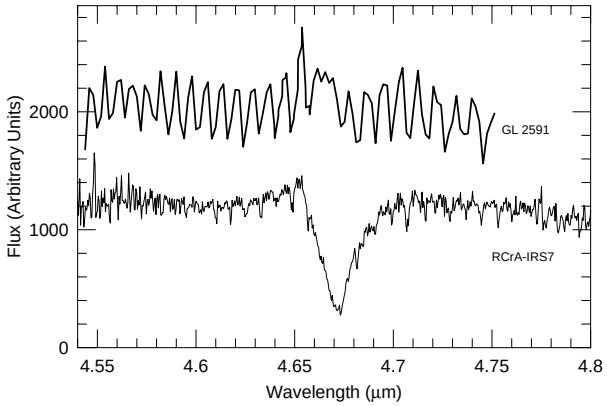

FIG. 5.—Spectrum of GL 2591 (*top*) showing gas-phase CO absorption lines compared to the spectrum of R CrA IRS 7 (*bottom*). This comparison shows that the narrow absorption lines in the spectrum of R CrA IRS 7 are due to gas-phase CO. The prominent emission feature at 4.654 μm in GL 2591 is the Pfβ hydrogen emission line. (Spectrum of GL 2591 from Tielens et al. 1991.)

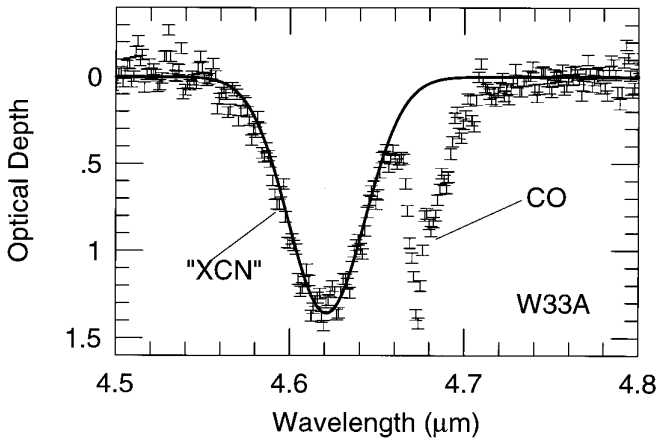

FIG. 6.—Spectrum of W33A in the wavelength region 4.5–4.8 μm. The "XCN" (4.62 μm) and CO (4.67 μm) features are labeled. The solid line is a Gaussian curve fitted to the "XCN" feature. This curve has been subtracted before attempting to fit the CO profile.

TABLE 5

ALTERNATIVE FITS FROM χ^2 ROUTINE[a]

Source	Nonpolar Mixture	Polar Mixture	χ_v^2
		Low-Mass Objects	
Elias 18.....	$CO:O_2:N_2:CO_2$ (100:50:25:32, 10 K)	$H_2O:CH_3OH$ + irr. (2:1, 10, 67 K)	5.6–7.0
	$CO:O_2:CO_2$ (100:50:21, 10 K)	$H_2O:CH_3OH$ + irr. (2:1, 10 K)	6.1
		$H_2O:CO$ (4:1, 10–35 K)	6.6–7.7
	$CO:O_2:CO_2$ (100:50:16, 10 K)	$H_2O:CO$ (4:1, 10, 25 K)	7.7
L1489 IRS	$CO:O_2:N_2:CO_2$ (100:50:25:32, 10 K)	$H_2O:CO$ (4:1, 10–100 K)	1.7–1.8
	$CO_2:CO$ (20:1, 10 K)	$H_2O:CO$ (4:1, 10–100 K)	1.8–1.9
		$H_2O:CH_3OH$ + irr. (2:1, 10 K)	1.8
	$CO:CO_2$ + UV (100:50, 10 K)	$H_2O:CO$ (4:1, 35–100 K)	1.8–1.9
		$H_2O:CH_3OH$ + irr. (2:1, 10, 67 K)	1.8–2.0
	$CO:CO_2$ (100:21, 10 K)	$H_2O:CO$ (4:1, 10, 25 K)	2.0
	$CO:CO_2$ (100:23, 10 K)	$H_2O:CO$ (4:1, 10–100 K)	1.8–1.9
		$H_2O:CH_3OH$ + irr. (2:1, 10 K)	1.8
	$CO:CO_2$ (100:26, 10 K)	$H_2O:CO$ (4:1, 10–100 K)	1.8–2.0
		$H_2O:CH_3OH$ + irr. (2:1, 10 K)	1.8
	$CO:O_2:CO_2$ (100:50:16, 10 K)	$H_2O:CO$ (4:1, 10, 25 K)	2.0
	$CO:O_2:CO_2$ (100:50:21, 10 K)	$H_2O:CO$ (4:1, 10, 25, 100 K)	1.9
	$CO:O_2:CO_2$ (100:50:32, 10 K)	$H_2O:CO$ (4:1, 10–100 K)	1.7–1.9
		$H_2O:CH_3OH$ + irr. (2:1, 10 K)	1.8
	$CO:O_2:CO_2$ (100:20:11, 10 K)	$H_2O:CO$ (4:1, 10, 25 K)	2.0
	$CO:O_2:CO_2$ (100:11:20, 10 K)	$H_2O:CO$ (4:1, 10–100 K)	1.8–2.0
		$H_2O:CH_3OH$ + irr. (2:1, 10 K)	1.9
	$CO:O_2:CO_2$ (100:10:23, 10 K)	$H_2O:CO$ (4:1, 10–100 K)	1.7–2.0
		$H_2O:CH_3OH$ + irr. (2:1, 10 K)	1.8
	$CO:N_2:CO_2$ (100:50:20, 10 K)	$H_2O:CO$ (4:1, 10, 25 K)	2.0
		$H_2O:CH_3OH$ + irr. (2:1, 10, 67 K)	1.8–2.0
	$CO:O_2:N_2:CO_2:H_2O$ (25:25:10:13:1, 10 K)	$H_2O:CO$ (4:1, 10–100 K)	1.7–2.0
		$H_2O:CH_3OH$ + irr. (2:1, 10, 67 K)	1.7–1.9
	$CO:CO_2$ (100:23, 30 K)	$H_2O:CO$ (4:1, 10, 25 K)	1.9
	$CO:CO_2$ (100:26, 30 K)	$H_2O:CO$ (4:1, 10, 25 K)	1.9
	$CO:O_2:CO_2$ (100:50:16, 30 K)	$H_2O:CO$ (4:1, 10, 25 K)	1.9
	$CO:O_2:CO_2$ (100:50:21, 30 K)	$H_2O:CO$ (4:1, 10–35 K)	1.8–1.9
		$H_2O:CH_3OH$ + irr. (2:1, 10, 67 K)	1.9
	$CO:O_2:CO_2$ (100:10:23, 30 K)	$H_2O:CO$ (4:1, 10, 25 K)	1.9
	Pure CO (10 K) + irradiation	$H_2O:CO$ (4:1, 10, 25 K)	1.9
R CrA IRS 1	Pure CO	$H_2O:CO$ (4:1, 10–35 K)	3.9–5.1
		$H_2O:CH_3OH$ + irr. (10 K)	4.7
R CrA IRS 2	Pure CO (10 K)	$H_2O:CO$ (4:1, 10–100 K)	0.7–0.8
		$H_2O:CH_3OH$ + irr. (10, 67 K)	0.8
	$CO:O_2:CO_2$ (100:54:10, 10 K)	$H_2O:CO$ (4:1, 10, 25 K)	0.8
R CrA IRS 7	$CO:O_2:CO_2$ (100:50:21, 30 K)	$H_2O:CO$ (4:1, 10–35 K)	5.3–6.6
	$CO:O_2:CO_2$ (100:50:16, 30 K)	$H_2O:CO$ (4:1, 10, 25 K)	6.4
		High-Mass Objects	
W33A.....	Pure CO	$H_2O:CH_3OH$ + irr. (2:1, 10 K)	6.1
		$H_2O:CO$ (4:1, 35, 50 K)	7.2–8.4
	$CO:H_2O$ (10:1, 10 K)	$H_2O:CO$ (4:1, 100 K)	6.3
	$CO:O_2:N_2:H_2O$ (40:40:15:1, 30 K)	$H_2O:CH_3OH$ + irr (2:1, 10 K)	6.9
		$H_2O:CO$ (4:1, 35 K)	7.7
	$CO:N_2:H_2O$ (50:50:1, 30 K)	$H_2O:CH_3OH$ + irr (2:1, 10 K)	7.3
GL 961E	$CO:CO_2$ + UV (100:50, 10 K)	$H_2O:CO$ (20:1, 20, 30 K)	1.7–1.9
	$CO:CO_2$ (100:23, 10 K)	$H_2O:CO$ (20:1, 30 K)	1.9
	$CO:CO_2$ (100:26, 10 K)	$H_2O:CO$ (20:1, 20, 30 K)	2.0
	$CO:O_2:CO_2$ (100:50:32, 10 K)	$H_2O:CO$ (20:1, 10–30 K)	1.7–1.8
	$CO:O_2:CO_2$ (100:50:23, 10 K)	$H_2O:CO$ (20:1, 10–30 K)	1.9–2.0
	$CO:O_2:N_2:CO_2$ (100:50:25:32, 10 K)	$H_2O:CO$ (20:1, 10–30 K)	1.7–1.9
	$CO:O_2:N_2:CO_2:H_2O$ (25:25:10:13:1, 10 K)	$H_2O:CO$ (20:1, 20, 30 K)	1.7
Mon R2 IRS 2	$CO:H_2O$ (10:1, 10 K)	$H_2O:CO$ (20:1, 10–30 K)	3.0–3.4
		$H_2O:CO$ (4:1, 10–35 K)	3.0–3.4
	$CO_2:CO$ (20:1, 10 K)	$H_2O:CH_3OH$ + irr. (67 K)	3.1
		$H_2O:CO$ (20:1, 20–50 K)	3.3–3.8
	$CO:O_2:CO_2$ (100:54:10, 10 K)	$H_2O:CO$ (4:1, 10, 25 K)	3.4
	$CO:O_2:N_2:CO_2:H_2O$ (50:35:15:3:1, 10 K)	$H_2O:CO$ (4:1, 10, 25 K)	3.7
	$CO:O_2:CO_2$ (100:54:8, 10 K)	$H_2O:CO$ (4:1, 10, 25 K)	3.7
NGC 7538 IRS 9.....	$CO:H_2O$ (10:1, 10 K)	$H_2O:CO$ (4:1, 10–100 K)	3.0–3.9
		$H_2O:CO$ (20:1, 10–80 K)	3.0–3.5
		$H_2O:CH_3OH$ + irr. (10, 67 K)	3.0–3.4
	Pure CO (10 K)	$H_2O:CH_3OH$ + irr. (10 K)	3.4
		$H_2O:CO$ (4:1, 10, 25 K)	3.6
	$CO:O_2:CO_2$ (100:50:4, 10 K)	$H_2O:CO$ (4:1, 10, 25 K)	3.5
	$CO:O_2:H_2O$ (50:50:1, 30 K)	$H_2O:CO$ (4:1, 10, 25 K)	3.5

[a] This table lists all mixtures that provide fits comparable to the lowest χ_v^2 fit. See text for further explanation. The "best" fit for each source is listed first.

TABLE 6

DUST COLUMN DENSITIES (cm^{-2})

SOURCE	N(CO) ($\times 10^{17}$)			$N(H_2O)$ ($\times 10^{17}$)	$N(CO)/N(H_2O)$	A_V (mag)	N(H) GAS ($\times 10^{23}$)
	Nonpolar	Polar	Total				
Low-Mass Objects							
Elias 18	1.9 ± 0.2	1.3 ± 0.3	3.1 ± 0.3	14[a]	0.2	18.5	3.52
L1489 IRS	4.5 ± 0.7	1.7 ± 0.7	6.2 ± 1.0	47[b]	0.1	29	5.51
R CrA IRS 1	4.1 ± 0.2	2.5 ± 0.6	6.5 ± 0.6	24[c]	0.3	25	4.75
R CrA IRS 2	11 ± 3	0.6 ± 0.7	12 ± 3	21[d]	0.6	35	6.66
R CrA IRS 7	5.4 ± 0.2	4.6 ± 0.6	10 ± 1	60[d]	0.2	35	6.66
High-Mass Objects							
W33A	2.3 ± 0.2	6.6 ± 0.5	8.9 ± 0.5	90–420[e]	0.02–0.1	50–100	9.50–28.5
GL 961E	1.4 ± 0.2	1.5 ± 0.2	2.9 ± 0.3	40[f]	0.1	17	3.23
Mon R2 IRS 2	1.6 ± 0.1	1.2 ± 0.2	2.7 ± 0.2	45[f]	0.1	21	3.99
NGC 7538 IRS 9	11 ± 1	1.4 ± 0.8	12 ± 1	64[e]	0.2	84	16.0

NOTE.—Column densities are for the solid phase unless otherwise noted. Lower bound on H_2O ice column density for W33A is from saturated 3.0 μm feature; upper bound was estimated from 6.0 μm feature.

[a] Estimated from spectra in Whittet et al. 1988.

[b] Sato, Nagata, & Yamamoto 1990.

[c] Whittet et al. 1996.

[d] Tanaka et al. 1994.

[e] Allamandola et al. 1992.

[f] Smith et al. 1989.

feature. When present, the Pfβ hydrogen emission line at 4.654 μm was excluded from the wavelength region used for fitting. In the case of W33A, the XCN feature was "removed" before fitting the CO profile by fitting a Gaussian to the feature and subtracting it from the spectrum (Fig. 6).

Column densities for solid CO are calculated for the polar and nonpolar components of the CO feature using the equation $N = (\tau \Delta v/A)$ cm^{-2} (Table 6). The full width at half-maximum (Δv; cm^{-1}) and optical depth (τ) for each component are determined by the resulting fit to the astronomical spectrum; the band strength (A), determined from laboratory experiments, is only weakly dependent on the composition of the matrix (Gerakines et al. 1995) and is equal to 1.1×10^{-17} cm molecule^{-1} for polar and nonpolar CO.

4. LOW-MASS EMBEDDED OBJECTS

4.1. *Taurus: Elias 18, L1489 IRS*

Elias 18 appears to lie near the eastern edge of a dense condensation within the Taurus cloud, and it illuminates a visible reflection nebula (IC2087) to the west (see Fig. 9 of Elias 1978 and discussion therein). Its CO profile has previously been modeled, using a smaller database of laboratory mixtures, by Chiar et al. (1995). Elias 18 provides an important comparison to the other embedded objects in this paper, so the modeling of its CO profile is repeated here using all the currently available laboratory mixtures. The CO spectrum is broad in nature, with a significant contribution from the polar component. The best fit (Fig. 2, *upper left*) is given by $CO:O_2:N_2:CO_2$ (100:50:25:32, 10 K) and the irradiated mixture of $H_2O:CH_3OH$ (2:1, 67 K) for the nonpolar and polar components, respectively. Other good fits are also given by nonpolar mixtures that contain 10%–12% CO_2 (see Table 5). The fits are consistent with the one presented in Chiar et al. (1995), in which the profile was fitted by a mixture with a high CO_2 percentage.

L1489 IRS is a class I protostar, with an associated CO outflow (Rodriguez et al. 1989), embedded in the L1489 dense core in the Taurus dark cloud ($A_V \sim 29$ mag; Myers et al. 1987). We present the first detection of solid CO in this line of sight (Fig. 2, *upper right*). The profile is similar in shape to that of Elias 18. The best fit is given by a mixture with a substantial amount of CO_2, $CO:O_2:N_2:CO_2$ (100:50:25:32, 10 K) combined with $H_2O:CO$ (4:1, 100 K). Unfortunately, the low S/N of this spectrum makes it difficult to constrain the precise chemical composition of the CO-containing mantles; there are 80 fits that come within 20% of the lowest χ^2_ν value (Table 5). However, general conclusions may be drawn; all of the nonpolar mixtures that provide good fits (combined with various polar mixtures) contain large amounts of CO_2 (10%–52%) or are UV irradiated.

Our ground-based data strongly suggest the presence on CO_2 in embedded objects in Taurus. Direct detection of CO_2 in the quiescent cloud medium and toward embedded objects in Taurus has recently been accomplished by *ISO* (Whittet et al. 1998).

4.2. *R CrA IRS 1, IRS 2, IRS 7*

The YSOs R CrA IRS 1, IRS 2, and IRS 7 are embedded in the Corona Australis complex near the young star R Corona Austrina. R CrA IRS 1 (Strom, Strom, & Grasdalen 1974), is an intense infrared source associated with the Herbig-Haro nebula HH100. The source is located about 25″ northeast of the optical nebula but coincident with a peak in the line emission from dense molecular gas (Anglada et al. 1989). It is part of the newly formed star cluster embedded in the R CrA dark cloud. R CrA IRS 1 has a circumstellar disk (Bastien & Ménard 1990) and drives a bipolar outflow (Anglada et al. 1989). In comparison to other infrared sources associated with Herbig-Haro objects, the millimeter (1300 μm) flux of R CrA IRS 1 is low relative to its bolometric luminosity by at least a factor of 2 (Reipurth et al. 1993), indicating that it is no longer deeply embedded in accreting material. Thus, this source is probably a pre–main-sequence star that is situated behind a molecular core obscured by $\sim$25 mag of visual extinction

(Whittet et al. 1996). The CO spectrum of R CrA IRS 1, shown in the middle left panel of Figure 2, is best fit with pure CO combined with H_2O:CO (4:1, 10 K). Although various polar mixtures also provide good fits (along with pure CO) to the profile, only pure CO gives a reasonable fit to the nonpolar component. In fact, nonpolar mixtures with as little as 1% H_2O (combined with any of the polar mixtures) result in substantially poorer fits. A deep 4.27 μm CO_2 feature has recently been detected by *ISO* in this line of sight (Gerakines et al. 1998). As the CO profile does not show evidence for CO_2, it is likely that the CO_2 resides in a grain population separate from the CO. In other words, there is separation of processed and unprocessed grains along the line of sight.

Wilking, Taylor, & Storey (1986) have classified R CrA IRS 2 as a class I protostar; the object is surrounded by dust at a wide range of temperatures and is still deeply embedded in its placental cloud ($A_V \sim 35$ mag). The CO absorption toward R CrA IRS 2, previously detected by Tanaka et al. (1994), is saturated at the center of the feature. Our spectrum (Fig. 2, *middle right*) has high S/N in the wings of the profile, thus an estimate of the peak optical depth, $\tau_{4.67} = 4 \pm 1$ is predicted from the fitting results. This relatively narrow profile is best fit with pure CO and H_2O:CO (4:1, 100 K) to the nonpolar and polar components, respectively. The weakness of the broad feature makes it difficult to constrain the composition of the polar mantle component; any of the other polar mixtures provides comparable fits. IRS 2 also seems to lack the strong gas-phase absorption lines present in the spectra of IRS 1 and IRS 7. Although it is possible that gas-phase lines with a Doppler width less than 2 km s^{-1} (making the lines barely detectable; TTGB; Helmich 1996) could be present in the spectrum, comparison of the "wiggles" in the IRS 2 spectrum to positions of known gas-phase lines does not support this speculation.

R CrA IRS 7 is also classified as a class I protostar (Wilking et al. 1986); it is deeply embedded in the R CrA core obscured by $A_V > 35$ mag of extinction (Harju et al. 1993). Radio continuum observations reveal emission around the source and may represent shock-excited inner portions of a thick accretion disk surrounding a pre–main-sequence star with a stellar wind (Brown 1987). The CO spectrum of R CrA IRS 7 (Fig. 2, *lower left*) is broader in nature than that of R CrA IRS 1 and IRS 2 and is best fitted with CO:O_2:CO_2 (100:50:21, 30 K) combined with the polar mixture H_2O:CO (4:1, 10 K). This profile can also be fit with the nonpolar mixture above along with the polar mixtures H_2O:CO (4:1, 10–35 K). The available pure CO and nitrogen-containing mixtures result in significantly poorer fits to the data.

Diversity of chemical composition of the ice mantles between IRS 1, IRS 2, and IRS 7 could be related to the proximity of IRS 7 to the reflection nebulosity associated with the R CrA core; both IRS 1 and IRS 2 are located farther away from this central condensation. The CO profile may also reflect the different evolutionary stages of grain mantle growth toward these objects. This idea is discussed in more detail in § 6.

The amount of gas-phase CO for IRS 1 and IRS 7 cannot be directly determined from the infrared lines as they are not fully resolved. The spectrum of IRS 2 lacks detectable gas-phase lines; narrow lines, undetectable without echelle-grating resolution, could exist if there is no CO outflow along our line of sight. However, the lack of detectable gas-phase CO in the spectrum of IRS 2 could imply high CO depletion in the line of sight. Whereas toward IRS 1 and IRS 7, a significant amount of CO remains in the gas, much of the CO toward IRS 2 is in the solid phase (possibly as much as 50%). This conclusion is supported by the high CO/H_2O ratio for IRS 2 ($\sim$0.6, among the highest observed ratio in any source) compared to the much lower ratios for IRS 1 and IRS 7 ($\sim$0.1–0.2).

5. HIGH-MASS EMBEDDED OBJECTS

5.1. *W33A*

W33A is a highly luminous young stellar object ($L \sim 10^5$ $L_\odot$) deeply embedded in the W33 dense molecular cloud core ($A_V \sim$ 50–150 mag; Capps, Gillett, & Knacke 1978). Because of slightly lower resolution ($R \sim 1200$), the gas-phase lines in this spectrum are not as clearly separated as those in the R CrA sources. The best fit to the solid-state feature is achieved with a combination of Pure CO at 10 K and the irradiated mixture of H_2O:CH_3OH (2:1, 10 K) to the nonpolar and polar components, respectively. Comparable fits (Table 5) include nonpolar mixtures of pure CO or CO mixed with significant amounts of O_2 and N_2 and various warm ($T \geq 35$) or irradiated polar mixtures.

A higher resolution spectrum is necessary to fully account for the presence of gas-phase absorption lines in this spectrum; however, general conclusions regarding the composition of the mantles may be drawn. Our study suggests that there are two different grain populations toward W33A: a cold component, located in the denser more shielded region of the W33 molecular cloud, and a thermally processed component closer to the embedded object. High-resolution gas-phase CO observations have also shown two distinct temperature regimes along the line of sight, one at 23 K and one at 120 K (Mitchell, Allen, & Maillard 1988). W33A has the strongest XCN feature observed to date. As XCN is thought to be the product of energetic processing of simple N-containing ices (§ 1), the strong XCN feature is suggestive of a dust population that has been processed by irradiation, such as UV irradiation or ion bombardment (Lacy et al. 1984; Tegler et al. 1993). Methanol (3.54 μm; Allamandola et al. 1992) and CO_2 (4.27 μm; Gürtler et al. 1996), products of energetic processing, are also detected in W33A with abundances of 5% and $\sim$15% (Gerakines et al. 1998) relative to H_2O.

5.2. *GL 961E*

GL 961E is a B3-B2 zero-age main sequence star that is the exciting source of a compact H II region (Castelaz et al. 1985). The visual extinction for this source is $\sim$17 mag. The CO profile is best fitted with the nonpolar UV irradiated mixture of CO:CO_2 (100:50, 10 K) combined with a substantial contribution from the polar mixture H_2O:CO (20:1, 20 K). Comparable fits are also given by nonpolar mixtures that have a high percentage of CO_2 ($\sim$17%), combined with strong polar mixtures (H_2O:CO = 20:1, 10–30 K). Modeling of the H_2O ice feature (Smith et al. 1989) showed that the ice temperature is less than $\sim$30 K; this is consistent with the fit to the CO profile. Independent evidence for the presence of CO_2 in this line of sight is given by detection of the 15.2 μm CO_2 feature made via the low-resolution spectrometer (LRS) on board *IRAS* (d'Hendecourt & Jourdain de Muizon 1989). The fact that

the CO profile can be fitted with a CO_2-containing mixture means that CO and CO_2 may coexist in the same mantle layer. This is in contrast to the scenario proposed for the R CrA sources (IRS 1 and IRS 2) discussed above; in these sight lines, CO and CO_2 reside in separate grain populations.

5.3. *Mon R2 IRS 2*

Mon R2 IRS 2 is a protostellar source, obscured by ~ 21 mag of extinction, which illuminates a shell-like IR reflection nebula in the Monoceros R2 molecular cloud (Aspin & Walther 1990; Beckwith et al. 1976). The CO profile of Mon R2 IRS 2 is best fitted with a nonpolar mixture of $CO:H_2O$ (10:1, 10K) and a polar mixture of either $H_2O:CO$ (4:1, 10 or 25 K) or $H_2O:CO$ (20:1, 10 K). Some of the fits listed in Table 5 suggest that there are warm ($T \geq 35$ K) ices in this sight line; e.g., one fit utilizes a polar mixture of $H_2O:CO$ at 50 K. However, modeling of the 3 μm H_2O ice feature shows that the polar ice is at a temperature lower than ~ 30 K (Smith et al. 1989). Thus, the nature of the ice composition suggested by these fits (which use warm polar mixtures) are not as probable as that implied by the other fits.

5.4. *NGC7538 IRS 9*

IRS 9, a young stellar object deeply embedded in the NGC7538 molecular cloud, is associated with an infrared reflection nebula (Werner et al. 1979). Obscured by ~ 84 mag of extinction (Allamandola et al. 1992), this source is bipolar and is surrounded by a dust torus (Eiroa, Gomez, & Lenzen 1988). The CO profile is best fit with $CO:H_2O$ (10:1, 10 K) and $H_2O:CO$ (4:1, 100 K) for the nonpolar and polar features, respectively. Like W33A, gas-phase CO studies of NGC 7538 IRS 9 show both cold (26 K) and hot (180 K) gas components along this line of sight (Mitchell et al. 1990), consistent with the weakness of the polar component. Other comparable fits (Table 5) include $CO:O_2:CO_2$ (100:50:4, 10 K) with $H_2O:CO$ (4:1, 10 and 25 K). The nonpolar component dominates the CO feature in this line of sight suggesting that there is a grain population or mantle layer that is dominated by CO (possibly mixed with O_2).

CO_2, CH_3OH, and CH_4 have been detected in NGC 7538 IRS 9; abundances of these molecules, relative to H_2O ice, are calculated to be $\sim 15\%$ for CO_2 (de Graauw et al. 1996), $\sim 5\%$ for CH_3OH (Allamandola et al. 1992; Chiar, Adamson, & Whittet 1996), and 2% for CH_4 (Lacy et al. 1991; Boogert et al. 1996). If energetic processing produces CO_2 and CH_3OH along this sight line, these molecules probably exist in grain mantles closer to the embedded object. Energetic processing is most likely responsible for the production of XCN, which is also detected toward NGC 7538 IRS 9 (Pendleton et al. 1998). The CO-containing mantles are separated along the line of sight and probably reside in a more protected dust layer farther from the embedded object.

There do not appear to be any systematic differences in the CO fits between the high- and low-mass objects (see Table 4), except that XCN is present in a greater percentage of the high-mass objects. Both types of objects show evidence for distinct cold and processed grain components along the line of sight. Column densities for the CO and H_2O ice features are listed in Table 6. The CO/H_2O ratio appears to be fairly consistent among the high- and low-mass objects. With the exception of R CrA IRS 2, CO/H_2O is in the range 0–0.3 for both groups.

6. DISCUSSION: THE EVOLUTION OF ICY MANTLES

Past studies of the CO feature toward embedded objects in the Taurus dark cloud have shown that these objects have distinctly different CO profiles compared to the field stars. CO profiles for the embedded stars (e.g., Elias 1 and 18; Chiar et al. 1995) are broad in nature and show evidence for thermal processing of the grain mantles in the vicinity of the embedded object; whereas those of field stars show that the icy mantles in these sight lines are cold (and unprocessed) and the CO exists in (almost) pure form. Data for YSOs presented in this paper show that the CO profiles of embedded objects do not always reflect thermal or energetic processing of the mantles. Although it is expected that sight lines toward luminous embedded objects will sample processed dust, it is important to remember that, in many cases, there is also a quiescent cloud component that contributes to the observed features. In addition, our line of sight could intersect a circumstellar disk edge-on. With these possibilities in mind, it is not surprising that the same line of sight may show evidence for both processed and unprocessed ices.

One of the possible signatures of processed ices is a CO profile consistent with CO in a $CO:CO_2$ mixture (Tielens et al. 1991; Chiar et al. 1995; this paper, Table 4). First *direct* detection of solid CO_2 via the strong 4.27 μm C=O stretching resonance was achieved by *ISO* (de Graauw et al. 1996; Gürtler et al. 1996; d'Hendecourt et al. 1996). Results show that CO_2 is a ubiquitous constituent of ices in molecular clouds associated with embedded YSOs; the total line-of-sight abundance of CO_2 is typically 10%–20% of the H_2O abundance in sources studied to date (de Graauw et al. 1996). However, CO_2 is also seen in *field stars* toward the Galactic center (de Graauw et al. 1996) and the Taurus cloud (Whittet et al. 1997), indicating that the presence of a local embedded radiation source is not a prerequisite for the occurrence of CO_2 in the ices. This latter result requires a reassessment of the supposed mechanisms by which solid CO_2 forms in the interstellar medium (ISM); energetic processing of CO-rich or CH_3OH-rich ices (§ 1) is unlikely to be a major source of CO_2 in quiescent molecular clouds (unless processing by cosmic rays is sufficiently rapid). An alternative model proposes that interstellar CO_2 ice is formed through grain surface reactions of atomic O with CO (Tielens & Hagen 1982). The $CO/CO_2/H_2O/H_2CO/CH_3OH$ ratios reflect relative accretion rates and reaction probabilities on the grain surface (Tielens & Hagen 1982; Charnley et al. 1992). In this case, observed variations in the CO/CO_2 ratio are a natural consequence of the varying composition of the accreting gas resulting from, for example, density variations.

Embedded objects for which ice absorption data are available can be roughly divided into three groups, representing an evolutionary trend (Chiar 1997b). These are roughly illustrated in Figure 7, which plots the nonpolar CO column density versus the H_2O ice column density. Water ice column densities are from Willner et al. (1982), Eiroa & Hodapp (1989), Smith et al. (1989), Tanaka et al. (1990), and Table 6. Sources in which solid CO has been detected are represented in groups I and II. In group I, there is no evidence of processing of the CO-containing ices. As should be expected, the background objects Elias 16

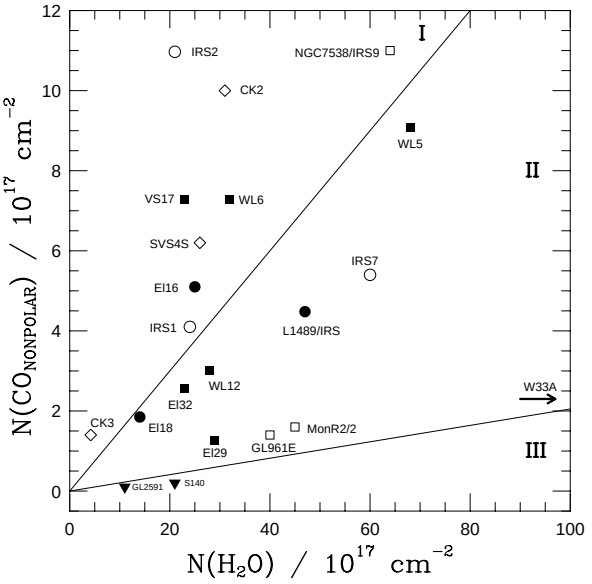

FIG. 7.—Plot of nonpolar CO column density versus H_2O ice column density for YSOs in several star-forming regions. Taurus, R CrA, Serpens, and ρ Oph sources are represented by filled circles, open circles, open diamonds, and filled squares, respectively. High-mass YSOs are represented by open squares and filled triangles (upper limits for nonpolar CO column density). The background stars Elias 16 (Taurus) and CK2 (Serpens) are shown for comparison. The solid lines divide the plot into three zones discussed in the text.

(Taurus) and CK2 (Serpens) are among the objects in this category, which occupy the area above the uppermost line in Figure 7. The CO spectrum is dominated by deep nonpolar CO and the polar component is weak (with the exception of SVS4S in Serpens). The ratio of CO/H_2O is relatively high (25%–60%) and XCN is not generally detected.[4] Carbon dioxide has been detected in Elias 16 (Whittet et al. 1998), NGC 7538 IRS 9 (de Graauw et al. 1996), R CrA IRS 1, IRS 2 (Boogert et al. 1998), and may exist in a separate grain population along the line of sight (Gerakines et al. 1998; Boogert et al. 1998).

In the intermediate cases, the CO/H_2O ratio is much smaller ($\sim$0%–20%). These sources are located in zone II in Figure 7. Polar CO accounts for 40%–50% of the total CO abundance for many of these sources. In some cases, the nonpolar component shows evidence for CO_2 (Elias 18, R CrA IRS 7, GL961E). Independent detection of CO_2 in R CrA IRS 7 (Boogert et al. 1998) and Elias 18 (Whittet et al. 1997) by *ISO* confirms its presence in the grain mantles. For objects such as IRS 7, CO_2 and CO may coexist in the same mantle layer. Zone II also consists of objects in which the nonpolar component can only be fitted with mixtures containing more than 90% CO (W33A, Mon R2 IRS 2, ρ Oph-Elias 29, Elias 32, WL5, WL12). Solid CO_2 has been detected by *ISO* in W33A (Gürtler et al. 1996); CO and CO_2 are probably spatially separated along the line of sight. The detection of XCN in R CrA IRS 7, W33A, GL961E, Mon R2 IRS 2, and Elias 18 is indicative of processing of the icy mantles in these sight lines (this work; Pendleton et al. 1998; Tegler et al. 1995).

[4] XCN is detected toward NGC 7538 IRS 9 (Pendleton et al. 1998). The ρ Oph and Serpens data do not have sufficient wavelength coverage to search for XCN.

The final group of embedded objects (zone III), contains two sources, S140 and GL 2591. In these objects, solid CO is not detected, but H_2O ice is known to be present (based on detection of the 3.1 μm H_2O ice feature). For these objects, the CO has been partially evaporated (confirmed through observations of gas-phase CO lines; e.g., Mitchell et al. 1989; van Dishoeck et al. 1996) and partly converted to CO_2 (and/or other species). *ISO* has confirmed the presence of CO_2 in these sight lines (de Graauw et al. 1996). Somewhat surprisingly, neither source has an XCN detection; more generally, all sources in which XCN has been detected also show solid CO. This suggests that XCN is a transient molecule that does not survive in the harsher environments of evolved protostars.

7. SUMMARY

We have analyzed the CO profiles of a sample of young stellar objects that span a range of mass and luminosity. Our χ^2 minimization routine and our procedure for determining a cutoff for acceptable fits show that several combinations of polar and nonpolar mixtures are capable of providing comparable matches to the observed profile. These "alternate" fits generally imply similar chemical composition and temperature for the ice mantles toward individual objects. In some sight lines, CO_2 and CO appear to be intimately mixed in the same mantle layer; whereas in others, modeling of the CO profile implies that CO exists in (nearly) pure form. Toward some sources in both groups, CO_2 has been independently detected by *ISO*, confirming its presence somewhere along the line of sight.

We have proposed an evolutionary scheme to explain the chemical diversity of the grain mantles in different sight lines. This scheme is based on comparison between the nonpolar CO column density, which traces the volatile CO-rich grain mantle, and the H_2O ice column density, which traces the total less volatile polar-ice column density. YSOs with ice detections are roughly divided into three groups: group I contains sources whose CO profiles are dominated by the nonpolar component, group II contains sources that have a relatively strong polar CO component, and the final group (III) contains sources in which CO is not detected.

There do not appear to be any systematic differences, in the CO profiles or column densities, between the high- and low-mass objects. However, presently the database of high-mass young stellar objects that have high-resolution ($R > 1200$) CO data is sparse. The evolutionary status of many high-mass YSOs is also not well known, making it more difficult to correlate the evolution of grain mantles with age. We have undertaken a study to observe a larger sample of YSOs in an effort to trace the affect of mass, age, and parent cloud on grain mantle evolution. Our studies, in conjunction with additional observational and laboratory investigations, of molecules such as NH_3, CH_4, CH_3OH, and CO_2, will help unravel the chemical and physical processes affecting grain mantle composition.

We would like to thank Tom Geballe and the UKIRT Service Programme for the observations of some of the data presented here. The service data were obtained in collaboration with D. Weintraub and S. Tegler. We are grateful to A. Chrysostomou for providing us with the W33A spectrum. UKIRT is operated by the Joint Astronomy Centre on behalf of the UK Particle Physics and Astronomy

Research Council. This work has made use of the Starlink Project software. J. E. C. currently holds a National Research Council-ARC Research Associateship. D. C. B. W. and J. E. C. acknowledge support from NASA grants NAG5 3339 (Long-Term Space Astrophysics) and NAGW 4039 (*Infrared Space Observatory*). A. J. A. is partly funded by the UK STARLINK project and partly by the University of Central Lancashire.

REFERENCES

Allamandola, L. J., Sandford, S. A., Tielens, A. G. G. M., & Herbst, T. M. 1992, ApJ, 399, 134
Allamandola, L. J., Sandford, S. A., & Valero, G. 1988, Icarus, 76, 225
Anglada, G., Rodriguez, L. F., Torrelles, J. M., Estalella, R., Ho, P. T. P., Canto, J., Lopez, R., & Verdes-Montenegro, L. 1989, ApJ, 341, 208
Aspin, C., & Walther, D. M. 1990, A&A, 235, 387
Bastien, P., & Ménard, F. 1990, ApJ, 364, 232
Beckwith, S., Evans, N. J., II, Becklin, E. E., & Neugebauer, G. 1976, ApJ, 208, 390
Bernstein, M. P., Sandford, S. A., Allamandola, L. J., Chang, S., & Scharberg, M. A. 1995, ApJ, 454, 327
Boogert, A. C. A., et al. 1996, A&A, 315, L377
———. 1998, in preparation
Brown, A. 1987, ApJ, 322, L31
Burton, M. 1992, Proc. Astron. Soc. Australia, 10, 52
Capps, R. W., Gillett, F. C., & Knacke, R. F. 1978, ApJ, 226, 863
Castelaz, M. W., Grasdalen, G. L., Hackwell, J. A., Capps, R. W., & Thompson, D. 1985, AJ, 90, 1113
Charnley, S. B., Tielens, A. G. G. M., & Millar, T. J. 1992, ApJ, 399, 71
Chen, W. P., & Graham, J. A. 1993, ApJ, 409, 319
Chiar, J. E. 1997a, Orig. Life Evol. Biosphere, 27, 79
———. 1997b, Ph.D. thesis, Rensselaer Polytechnic Institute
Chiar, J. E., Adamson, A. J., Kerr, T. H., & Whittet, D. C. B. 1994, ApJ, 426, 240
———. 1995, ApJ, 455, 234
Chiar, J. E., Adamson, A. J., & Whittet, D. C. B. 1996, ApJ, 472, 665
Chrysostomou, A., Hough, J. H., Whittet, D. C. B., Aitken, D. K., Roche, P. F., & Lazarian, A. 1996, ApJ, 461, L61
de Graauw, Th., et al. 1996, A&A, 315, 345
d'Hendecourt, L. B., Allamandola, L. J., Grim, R. J. A., & Greenberg, J. M. 1986, A&A, 158, 119
d'Hendecourt, L. B., & Jourdain de Muizon, M. 1989, A&A, 223, L5
d'Hendecourt, L. B., et al. 1996, A&A, 315, L365
Ehrenfreund, P., Boogert, A. C. A., Gerakines, P. A., Jansen, D. J., Schutte, W. A., Tielens, A. G. G. M., & van Dishoeck, E. F. 1996, A&A, 315, 341
Ehrenfreund, P., Boogert, A. C. A., Gerakines, P. A., Tielens, A. G. G. M., & van Dishoeck, E. F. 1997, A&A, 328, 649
Eiroa, C., Gomez, A. I., & Lenzen, R. 1988, A&A, 190, 283
Eiroa, C., & Hodapp, K.-W. 1989, A&A, 210, 345
Elias, J. H. 1978, ApJ, 224, 857
Elsila, J., Allamandola, L. J., & Sandford, S. A. 1997, ApJ, 479, 818
Geballe, T. R. 1986, A&A, 162, 248
Gerakines, P. A., Schutte, W. A., & Ehrenfreund, P. 1996, A&A, 312, 289
Gerakines, P. A., Schutte, W. A., Greenberg, J. M., & van Dishoeck, E. F. 1995, A&A, 296, 810
Gerakines, P. A., et al. 1998, in preparation
Graham, J. A., & Chen, W. P. 1991, AJ, 102, 1405
Grim, R. J. A., & Greenberg, J. M. 1987, ApJ, 321, L91
Gürtler, J., Henning, Th., Kömpe, C., Pfau, W., Krätschmer, W., & Lemke, D. 1996, A&A, 315, 189
Harju, J., Haikala, L. K., Mattila, K., Mauersberger, R., Booth, R. S., & Nordh, H. L. 1993, A&A, 278, 569
Helmich, F. P. 1996, Ph.D. thesis, Univ. Leiden
Kerr, T. H., Adamson, A. J., & Whittet, D. C. B. 1993, MNRAS, 262, 1047
Lacy, J. H., Bass, F., Allamandola, L. J., Persson, S. E., McGregor, P. J., Lonsdale, C. J., Geballe, T. R., & van de Bult, C. E. P. M. 1984, ApJ, 276, 533
Lacy, J. H., Carr, J. S., Evans, N. J., II, Baas, F., Achtermann, J. M., & Arens, J. F. 1991, ApJ, 376, 556
Larson, H. P., Davis, D. S., Black, J. H., & Fink, U. 1985, ApJ, 299, 873
Marraco, H. G., & Rydgren, A. E. 1981, AJ, 86, 62
Mitchell, G. F., Allen, M., & Maillard, J.-P. 1988, ApJ, 333, 55
Mitchell, G. F., Curry, C., Maillard, J.-P., & Allen, M. 1989, ApJ, 341, 1020
Mitchell, G. F., Maillard, J.-P., Allan, M., Beer, R., & Belcourt, K. 1990, ApJ, 363, 554
Myers, P. C., Fuller, G. A., Mathieu, R. D., Beichman, C. A., Benson, P. J., Schild, R. E., & Emerson, J. P. 1987, ApJ, 319, 340
Palumbo, M. E., & Strazzulla, G. 1993, A&A, 269, 568
Pendleton, Y. J., Tielens, A. G. G. M., Tokunaga, A. T., & Bernstein, M. P. 1998, ApJ, submitted
Reipurth, B., Chini, R., Krugel, E., Kreysa, E., & Sievers, A. 1993, A&A, 273, 221
Rodriguez, L. F., Myers, P. C., Cruz-Gonzalez, I., & Terebey, S. 1989, ApJ, 347, 461
Sandford, S. A., & Allamandola, L. J. 1990, ApJ, 355, 357
Sandford, S. A., Allamandola, L. J., Tielens, A. G. G. M., & Valero, G. J. 1988, ApJ, 329, 498
Sato, S., Nagata, M., & Yamamoto, T. 1990, ApJ, 359, 192
Schmitt, B., Greenberg, J. M., & Grim, R. J. A. 1989, ApJ, 340, L33
Schutte, W. A., & Greenberg, J. M. 1997, A&A, 317, L43
Smith, R. G., Sellgren, K., & Tokunaga, A. T. 1989, ApJ, 344, 413
Strom, K. M., Strom, S. E., & Grasdalen, G. L. 1974, ApJ, 187, 83
Tanaka, M., Nagata, T., Sato, S., & Yamamoto, T. 1994, ApJ, 430, 779
Tanaka, M., Sato, S., Nagata, T., & Yamamoto, T. 1990, ApJ, 352, 724
Taylor, K. N. R., & Storey, J. W. V. 1984, MNRAS, 209, 5P
Tegler, S. C., Weintraub, D. A., Allamandola, L. J., Sandford, S. A., Rettig, T. W., & Campins, H. 1993, ApJ, 411, 260
Tegler, S. C., Weintraub, D. A., Rettig, T. W., Pendleton, Y. J., Whittet, D. C. B., & Kulesa, C. A. 1995, ApJ, 439, 279
Tielens, A. G. G. M., & Hagen, W. 1982, A&A, 114, 245
Tielens, A. G. G. M., Tokunaga, A. T., Geballe, T. R., & Baas, F. 1991, ApJ, 381, 181 (TTGB)
van Dishoeck, E. F., et al. 1996, A&A, 315, L349
Werner, M. W., Becklin, E. E., Gatley, I., Matthews, K., Neugebauer, G., & Wynn-Williams, C. G. 1979, MNRAS, 188, 463
Whittet, D. C. B., Adamson, A. J., Duley, W. W., Geballe, T. R., & McFadzean, A. D. 1989, MNRAS, 241, 707
Whittet, D. C. B., Adamson, A. J., McFadzean, A. D., Bode, M. F., & Longmore, A. J. 1988, MNRAS, 233, 321
Whittet, D. C. B., & Blades, J. C. 1980, MNRAS, 191, 309
Whittet, D. C. B., Bode, M. F., Longmore, A. J., Baines, D. W. T., & Evans, A. 1983, Nature, 303, 218
Whittet, D. C. B., Longmore, A. J., & McFadzean, A. D. 1985, MNRAS, 216, 45P
Whittet, D. C. B., et al. 1996, ApJ, 458, 363
———. 1998, ApJ, submitted
Wilking, B. A., Taylor, K. N. R., & Storey, J. W. V. 1986, AJ, 92, 103
Willner, S. P., et al. 1982, ApJ, 253, 174

Note added in proof.—After our paper went to press, we became aware of the paper by Teixera, Emerson, & Palumbo (A&A, 330, 711 [1998]); their work is a valuable addition to the database of solid CO profile analyses.